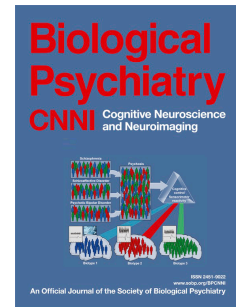


Accepted Manuscript

Awake mouse imaging: from 2-photon microscopy to BOLD fMRI

Michèle Desjardins, Kivılcım Kılıç, Martin Thunemann, Celine Mateo, Dominic Holland, Christopher G.L. Ferri, Jonathan A. Cremonesi, Baoqiang Li, Qun Cheng, Kimberly L. Weldy, Payam A. Saisan, David Kleinfeld, Takaki Komiyama, Thomas T. Liu, Robert Bussell, Eric C. Wong, Miriam Scadeng, Andrew K. Dunn, David A. Boas, Sava Sakadžić, Joseph B. Mandeville, Richard B. Buxton, Anders M. Dale, Anna Devor



PII: S2451-9022(18)30324-0

DOI: <https://doi.org/10.1016/j.bpsc.2018.12.002>

Reference: BPSC 364

To appear in: *Biological Psychiatry: Cognitive Neuroscience and Neuroimaging*

Received Date: 12 July 2018

Revised Date: 26 October 2018

Please cite this article as: Desjardins M., Kılıç K., Thunemann M., Mateo C., Holland D., Ferri C.G.L., Cremonesi J.A., Li B., Cheng Q., Weldy K.L., Saisan P.A., Kleinfeld D., Komiyama T., Liu T.T., Bussell R., Wong E.C., Scadeng M., Dunn A.K., Boas D.A., Sakadžić S., Mandeville J.B., Buxton R.B., Dale A.M. & Devor A., Awake mouse imaging: from 2-photon microscopy to BOLD fMRI, *Biological Psychiatry: Cognitive Neuroscience and Neuroimaging* (2019), doi: <https://doi.org/10.1016/j.bpsc.2018.12.002>.

This is a PDF file of an unedited manuscript that has been accepted for publication. As a service to our customers we are providing this early version of the manuscript. The manuscript will undergo copyediting, typesetting, and review of the resulting proof before it is published in its final form. Please note that during the production process errors may be discovered which could affect the content, and all legal disclaimers that apply to the journal pertain.

Awake mouse imaging: from 2-photon microscopy to BOLD fMRI

Abbreviated title: Imaging across scales in awake mouse

Michèle Desjardins^{1*#}, Kivılcım Kılıç^{2*†}, Martin Thunemann¹, Celine Mateo³, Dominic Holland², Christopher G.L. Ferri², Jonathan A. Cremonesi⁴, Baoqiang Li⁵, Qun Cheng², Kimberly L. Weldy², Payam A. Saisan², David Kleinfeld^{3,6,7}, Takaki Komiyama^{2,6}, Thomas T. Liu¹, Robert Bussell¹, Eric C. Wong¹, Miriam Scadeng¹, Andrew K. Dunn⁸, David A. Boas⁹, Sava Sakadžić⁵, Joseph B. Mandeville⁵, Richard B. Buxton¹, Anders M. Dale^{1,2}, Anna Devor^{1,2,5}

¹Department of Radiology, University of California San Diego, La Jolla, CA 92093, USA

²Department of Neurosciences, University of California San Diego, La Jolla, CA 92093, USA

³Department of Physics, University of California San Diego, La Jolla, CA 92093, USA

⁴Biology Undergraduate Program, University of California San Diego, La Jolla, CA 92093, USA

⁵Martinos Center for Biomedical Imaging, MGH, Harvard Medical School, Charlestown, MA 02129, USA

⁶Section of Neurobiology, University of California San Diego, La Jolla, CA 92093, USA

⁷Department of Electrical and Computer Engineering, University of California San Diego, La Jolla, CA 92093, USA

⁸Department of Biomedical Engineering, University of Texas at Austin, Austin, TX 78712, USA

⁹Department of Biomedical Engineering, Boston University, Boston, MA 02215, USA

*These authors equally contributed to this work.

#Present Address: Département de physique, de génie physique et d'optique, Université Laval and Centre de recherche du CHU de Québec – Université Laval, axe Oncologie, Québec, QC G1V 0A6, Canada;

†Present Address: Department of Biomedical Engineering, Boston University, Boston, MA 02215, USA

Key words: 2-photon microscopy; fMRI; Blood Oxygen Level Dependent (BOLD) signal; intrinsic optical signals; cerebral blood flow; optogenetic

Corresponding author:

Michèle Desjardins

2705, boulevard Laurier, Québec (Québec), Canada G1V 4G2

Tel: (418) 525-4444 #47531 or (418) 656-2131 #402783

Email: michele.desjardins@phy.ulaval.ca

Number of words in the abstract: 236

Number of words in the text (excluding abstract, acknowledgments and financial disclosures sections, legends, and references): 3661

Number of tables: 0

Number of figures: 5

Number of supplementary material: 7 (in a single, separate file: 5 figures, 1 movie, Methods)

ACCEPTED MANUSCRIPT

Abstract

Background. Functional Magnetic Resonance Imaging (fMRI) in awake behaving mice is well positioned to bridge the detailed cellular-level view of brain activity, which has become available due to recent advances in microscopic optical imaging and genetics, to the macroscopic scale of human noninvasive observables. However, while microscopic (e.g., 2-photon imaging) studies in behaving mice have become a reality in many laboratories, awake mouse fMRI remains a challenge. Furthermore, due to variability in behavior between animals, performing all types of measurements within the same subject is highly desirable and can lead to higher scientific rigor. **Methods.** Here, we demonstrate Blood Oxygenation Level Dependent (BOLD) fMRI in awake mice implanted with chronic “cranial windows” that allow optical access for microscopic imaging modalities and optogenetic (OG) stimulation. We start with 2-photon imaging of single-vessel diameter changes (N=1). Next, we implement intrinsic optical imaging of blood oxygenation and flow combined with laser speckle imaging of blood flow obtaining a “mesoscopic” picture of the hemodynamic response (N=16). Then, we obtain corresponding BOLD fMRI data (N=5). All measurements can be performed in the same mice in response to identical sensory and OG stimuli. **Results.** The cranial window does not deteriorate the quality of fMRI and allows alternating between imaging modalities in each subject. **Conclusions.** This report provides a proof of feasibility for multiscale imaging approaches in awake mice. In the future, this protocol can be extended to include complex cognitive behaviors translatable to humans, such as sensory discrimination or attention.

Introduction

Noninvasive imaging technologies such as functional Magnetic Resonance Imaging (fMRI), Positron Emission Tomography (PET) and Electro/Magnetoencephalography (EEG/MEG) are widely used to investigate the function of the human brain. However, interpretation of these macroscopic signals in terms of the underlying microscopic physiology, such as electrical activity of single neurons and hemodynamic activity of single blood vessels, is still under investigation (1). Noninvasive imaging in experimental animals can play a critical role in physiological underpinning and data-driven modeling of human noninvasive signals, in particular when both micro- and macroscopic measurements are achieved in the same subject under analogous experimental conditions.

The idea is to utilize state-of-the-art microscopic measurement technologies in the mouse to precisely and quantitatively probe concrete microscopic physiological parameters underlying macroscopic cerebral blood flow, O_2 consumption, and electrophysiological EEG/MEG signals, while manipulating cell-type-specific neuronal activity (1). These measurements, which are only available in animals, provide the data needed for building computational bridges across spatial scales and imaging/recording modalities. For example, these microscopic measurements can be used to simulate the Blood Oxygenation Level Dependent (BOLD) fMRI signal “bottom-up” (2-5). The endpoint result can then be validated against the actual mouse fMRI data (2). These simulations also provide the microscopic “ground truth” for the development and calibration of “top-down” macroscopic analytical fMRI models applicable to humans (6).

Our previous studies relied on fMRI data from anesthetized rodents. However, anesthesia can differentially affect neuronal cell types – as well as blood flow and O_2 metabolism – altering neuronal network activity and neuro-vascular-metabolic coupling. To this end, the current report provides a protocol and a proof of feasibility for BOLD fMRI in awake mice implanted with chronic glass “cranial windows” that do not significantly deteriorate the

quality of fMRI. These windows provide optical access for micro- and “mesoscopic” optical imaging modalities and neuronal stimulation with light (a.k.a. “optogenetics” (7)). Therefore, alternating between the imaging modalities for each subject is possible.

Mice have become the species of choice for detailed, microscopic *in vivo* imaging studies of the mammalian brain. This is in part due to recent advances in transgenic technology that allow genetically-targeted observation and manipulation of specific neuronal cell types. Novel genetically encoded probes of brain activity (e.g., genetically encoded calcium indicators, GECIs), as well as tools for optogenetic (OG) neuronal excitation and inhibition, have enabled new experimental paradigms where awake mice undergo repeated microscopic imaging, for the duration of weeks and months, while performing behavioral tasks (8). These chronic imaging studies are free from confounds of anesthesia and have a higher potential for human translation.

While optical imaging studies in awake and behaving mice have become routine, their fMRI counterpart remains a challenge. Prior studies have leveraged the power of noninvasive fMRI in intact conscious rodents to map the brain response to drug administration (9) and sensory stimuli, including tactile (10) and nociceptive somatic inputs (11) as well as odorants (12) and conditioned visual stimuli (13). Following the first demonstration of feasibility for combining fMRI with optogenetics by Lee and colleagues (14), the repertoire of stimuli applicable to awake rodent fMRI has been extended to include OG excitation or inhibition (15-19). In these studies, the OG light stimulus was delivered via an optical fiber implanted into the brain. In the present study, we employ a chronic cranial window that allows OG stimulation as well as single- and multiphoton optical imaging of the cortical area within the window, enabling multiscale/multimodal imaging for each experimental subject. First, we describe installation and stability of our MRI-compatible headpost assembly including the cranial window. Then, we provide example data using optical imaging and fMRI in response to OG and sensory stimuli. In the present study, we used a simple air puff sensory stimulus. In the future, this protocol can be

extended to include more complex cognitive behaviors translatable to humans, such as sensory discrimination or attention.

ACCEPTED MANUSCRIPT

Methods

Some of the procedures were similar to those described in our previous study (20). For brevity, only novel aspects are described here. Detailed methods can be found in the **Supplementary Methods**.

Animal procedures

The surgical procedure was modified from that previously described by the Anderman lab (21) (see **Supplementary Methods** for details). The left barrel cortex was exposed over a 3-mm diameter circle area with the center coordinates of A-P 2 mm and L-R 3 mm (relative to Bregma) and sealed with the glass window implant (**Fig. 1A**). A plastic headpost, used for immobilization of the head during imaging, was glued to the bone contralateral to the glass implant (**Fig. 1B**). To standardize the position of the imaging window across subjects, the headpost was lowered onto the bone while mounted onto a stereotactic manipulator ensuring a fixed angle and orientation.

Imaging

Following behavioral training, the animals were imaged using two-photon microscopy for single-vessel diameter measurements, spectral and laser speckle (LS) contrast imaging to measure blood oxygenation and flow, and BOLD fMRI. The BOLD fMRI methods are presented below; other methods can be found in the **Supplementary Methods**.

BOLD fMRI

MR images were acquired on a 7T/11 cm horizontal bore scanner (BioSpec 70/20 USR, Bruker) 7T scanner equipped with a BGA 12S2 gradient set with 440 mT/m gradient strength and 3440 T/m/s slew rate. A custom-made 2x3 cm diameter surface RF coil was used to transmit and receive the radiofrequency signal. BOLD fMRI data were acquired using a single-shot gradient-echo (GE) echo planar imaging (EPI) pulse sequence with the following parameters: TE/TR/FA = 11-20 ms / 1 s / 45°, matrix = 100 (Read, L/R) x 50 (PE, S/I) over a 2x1 cm FOV, slice thickness = 1 mm, 5 adjacent coronal slices in interleaved order. High-

resolution Rapid Acquisition with Relaxation Enhancement (TurboRARE) structural images were obtained of the same slices to identify brain structures and the location of the optical window (**Supplementary Fig. S5**). TurboRARE images had the same slice thickness as EPI images but higher in-plane resolution (256x128 for TurboRARE vs. 100x50 for EPI).

Mice were briefly (< 60s) anesthetized during the head fixation in a custom-made MRI-compatible mouse cradle (**Supplementary Fig. S1C**) and insertion of ear plugs (cut from commercial human-size silicon ear plugs). Once in the bore, coil stability was insured by inflating three pneumatic air chambers of the cradle to absorb vibrations. After manual coil matching and tuning, images were acquired in the following order: an anatomical localizer (TurboRARE), GE-EPI functional scans, spin-echo (SE) in forward and reverse directions for distortion correction (see below).

Motion correction was implemented by aligning each EPI image in a time series to the first one using in-house written rigid body registration software based on *imregister* Matlab function. Correction of image distortion due to B_0 field inhomogeneity induced by magnetic susceptibility variations was implemented using our previously published method that involves acquisition of two SE images with opposite phase encoding directions (22). EPI images were spatially smoothed with a 3-pixel FWHM Gaussian kernel. Ratio images were defined relative to a pre-stimulus baseline (2 s for event-related design, 5 s for blocked design) and averaged over stimulus trials. Realigned, smoothed images were entered into a general linear model (GLM) using SPM12 (Wellcome Trust Centre for Neuroimaging) and a canonical HRF with time derivatives. Using a finite impulse response model (FIR) yielded very similar results (not shown). A T-statistic contrast was used to identify voxels where the signal significantly differed from baseline, i.e. activated voxels. The statistical map was thresholded at $p = 0.001$ uncorrected to define an ROI for time-course extraction.

Stimulus paradigm

For sensory stimulation, each trial consisted of a 2-s train of air puffs at 3 Hz delivered to the lower bottom part of the contralateral whisker pad to avoiding an eye blink; we used 10 trials per run with 20-s inter-stimulus interval, ISI. For the blocked stimulus, the puffs were delivered at 5 Hz for 20 s. During OG stimulation, each trial consisted of a train of 5-ms blue light pulses delivered at 100 Hz during 100 ms (equivalent to a single 100-ms pulse at 50% duty-cycle); we used 10 trials per run with 20-s ISI. For the blocked stimulus, the 100-ms trains were repeated at 1 Hz for 20 s with 8 trials per run. In fMRI and IOI/SC imaging, the OG light was delivered to the surface of the window by means of an optical fiber placed ~0.5 mm above the glass window creating a ~1 mm circular illumination spot. In 2-photon experiments, the OG light was delivered through the objective (20). Laser power was 6-8 mW under the objective (for 2-photon imaging) or at the fiber tip (for OIS/LS imaging). In the control experiments in wild type mice, laser power at the tip of the fiber was 12 mW.

Results

The goal for this study was to establish a protocol for chronic imaging of awake behaving mice using different measurement modalities, including 2-photon imaging and fMRI, in each subject. Our criteria for success were as follows: (1) sufficient optical clarity of the window to allow 2-photon imaging throughout the cortical depth as well as single-photon imaging; (2) minimal loss of the BOLD fMRI signal due to unwanted susceptibility artifacts; (3) sufficient mechanical stability of the MRI-compatible headpost assembly to allow state-of-the-art 2-photon imaging under analogous head fixation to that used in fMRI experiments; (4) stability over time for longitudinal imaging for the duration of weeks and months; (5) compatibility with behavioral experiments. Below, we describe our design and illustrate the imaging capabilities.

MRI-compatible headpost assembly

We used glass window implants previously described by Mark Anderman's lab (21). The implant was prepared ahead of time and consisted of three 3-mm round coverslips and a single 5-mm coverslip, all made of borosilicate glass (#1 thickness, Warner Instruments 64-0720 (CS-3R) and 64-0700 (CS-5R)) and glued together using optical adhesive (NOA61, Norland) that was cured with UV light (Spot Cure-B6, Kinetic Instruments) (**Fig. 1A**). The headpost, needed for immobilization of the mouse head during imaging, was custom machined from polyether ether ketone (PEEK), an MRI-compatible hard plastic material (**Fig. 1B**). Premade glass window implants and PEEK headposts were kept in 70% ethanol until implantation.

Borosilicate glass differs from the brain tissue (mostly composed of H₂O) in its magnetic susceptibility index (23). For 2D pulse sequences using relatively thick slices (in our case, 1 mm), this mismatch can lead to a susceptibility signal loss due to within-voxel, through-plane variation of the B₀ field. Therefore, we standardized the position of the imaging window to ensure alignment of the glass/brain interface with the B₀ vector of the MRI scanner. To this end, the window and the headpost were fixed to the skull in a predetermined orientation such that,

when the mouse head was immobilized in the MRI “cradle”, the normal to the window plane would be orthogonal to B_0 (see **Methods**). In this way, susceptibility artifacts due to the window were limited to the perimeter of the implant.

In agreement with previous studies that utilized this type of cranial implants for 2-photon imaging (21), the window remained clear and transparent for the duration of weeks and months (**Fig. 1C**) allowing imaging throughout the cortical depth and down to the white matter (**Fig. 1D**). The quality of BOLD fMRI images depended to a large extent on the quality of the surgical preparation. Even after weeks of healing, residues of dry blood on the skull around the implant created signal loss and image distortion due to B_0 field inhomogeneity induced by magnetic susceptibility variations. Image distortion was corrected using our previously published method that involves acquisition of spin-echo (SE) echo-planar imaging (EPI) scans with opposite phase encoding polarities (22). Reversing the phase encoding direction resulted in opposite spatial distortion patterns. These data were then used to recover the correct image geometry of the target gradient-echo (GE) EPI scan (**Fig. 1E** and **Supplementary Fig. S1A-B**).

In all cases, BOLD fMRI images experienced some degree of signal loss at the edge of the borosilicate glass implant (**Fig. 1E**, red arrows). This artifact, however, was well localized to the perimeter of the window and did not significantly affect the quality of the BOLD signal immediately under the implant.

Compatibility with optical imaging across scales

Cranial glass windows allow optical imaging across scales that can be very informative for physiological underpinning of fMRI signals (20, 24, 25), in particular when the fMRI study is conducted in the same animal subject. On the microscopic scale, neuronal, glial, vascular and metabolic activity can be measured with sub-micron resolution using 2-photon imaging. **Figure 2A-C** illustrates an example of time-resolved imaging of single-vessel dilation, which is a key parameter in detailed models of fMRI signals (2, 6). These data were obtained by an

intravascular injection of a fluorescent contrast agent (FITC or Alexa 680 conjugated to dextran, see **Supplementary Methods**) and tracking the vessel diameter as a function of time. In this example, we used a VGAT-ChR2(H134R)-EYFP mouse where all inhibitory interneurons expressed the OG actuator Channelrhodopsin-2 (ChR2) (26). The OG stimulus consisted of a single 100-ms pulse of blue (473 nm) light delivered through the objective (20). In addition, we used a sensory stimulus, which consisted of three air puffs delivered at 3 Hz to the whisker pad contralateral to the imaging window. If desired, 2-photon imaging can be used to extract other parameters including measures of neuroglial activity (24, 27-29), intravascular or tissue oxygenation (30-34), O₂ consumption (35), and glucose metabolism (36). **Figure 2D-E** and **Supplementary Figure S2A** show the corresponding mesoscopic changes in blood oxygenation and flow obtained in the same subject under the same stimulus conditions using single-photon CCD-based imaging. In this example, we used simultaneous hemoglobin-based optical intrinsic signals (OIS) imaging and LS contrast imaging (37-39) to obtain changes in oxyhemoglobin (HbO), deoxyhemoglobin (HbR) and blood flow in response to OG and sensory stimulation. The OG stimulus was delivered via an optical fiber positioned ~0.5 mm above the window at an angle of ~60 degrees to avoid reflection from the glass surface (**Fig. 2D**) using the same stimulus parameters as for 2-photon imaging shown in **Figure 2C**. Presenting the same OG stimulus in wild type animals did not cause significant HbO/HbR changes (**Supplementary Fig. S2B**), arguing against potential effects of heat generated by the 473-nm laser within our range of laser power (40, 41). The sensory stimulus was the same as for 2-photon measurements (**Fig. 2C**). For 2-photon imaging, we rejected stimulus trials with large motion artifacts that could be identified by analysis of the surveillance video (see **Methods**) and/or unrealistically large signal changes. Sensory stimuli generated motion more often compared to OG stimuli: ~15-20% of trials were rejected for sensory stimuli and ~5-10% - for OG stimuli. OIS imaging is more robust against motion artifacts, thus no trials were rejected. Some studies used sedation to mitigate motion artifacts (27). In our hands, however, sedation with 1-2 mg/kg

chlorprothixene (Sigma-Aldrich) notably slowed down the hemodynamic response kinetics (**Supplementary Fig. S2C**). Thus, sedation is not recommended as a means of providing image stability in quantitative hemodynamic and neurovascular coupling studies.

BOLD fMRI in mice with chronic cranial windows

Mesoscopic OIS and LS contrast measures can serve as a proxy for the BOLD fMRI signal (42-45). However, the measurement theory for each of these measurement modalities is unique, relying on different assumptions across different imaging modalities (46). Therefore, direct acquisition of the fMRI data is highly desirable to ensure consistency of the modeling/integration framework (1, 2). To this end, we performed BOLD fMRI in mice with chronic cranial windows in response to OG and sensory stimulation. OG stimulus was delivered via an optical fiber similar to that used in the OIS/LS experiments. The fiber was positioned in the middle of the RF coil ending ~0.5 mm above the glass window at an angle of ~70 degrees (see **Methods** and **Supplementary Fig. S1C**). Since we used a small surface RF coil to transmit and receive (see **Methods**), our sensitivity dropped with distance from the coil resulting in an inhomogeneous signal-to-noise ratio (SNR) within the image. Therefore, we thresholded EPI images at ~40% of the maximum intensity to limit our analysis to pixels with high SNR. **Figure 3** illustrates BOLD fMRI responses to a 20-s train of 100-ms light pulses delivered at 1 Hz (**Fig. 3A-C**, analogous to a blocked design) and a single 100-ms light pulse (**Fig. 3D-E**, analogous to an event-related design) from a single fully awake Emx1-Cre/Ai32 subject where ChR2 was expressed in pyramidal cells (47, 48). BOLD ratio images (**Fig. 3A, D**) were calculated relative to the pre-stimulus baseline using a single slice cutting through the center of the evoked response. This presentation facilitates the comparison with OIS imaging if needed (25). The BOLD signal change in response to both stimulus conditions localized to the cortical tissue within the cranial window. The same data can also be viewed as p-value maps;

statistically significant activation localized to the cortical area within the window was detected for the blocked design (**Fig. 3C**). Time-courses extracted from the active ROI, which was defined by thresholding of the p-value map, revealed a high degree of temporal signal fluctuation (**Fig. 3B,E** and **Supplementary Fig. S3**), most likely due to spontaneous neuronal activity (49, 50) as well as residual movement artifacts. On average, an increase in the BOLD signal was visible for both stimulus conditions (thick lines in **Fig. 3B,E** and **Supplementary Fig. S3**). Comparison of the BOLD response time-course to that obtained by OIS/LS imaging revealed a consistent shape across the measurement modalities for the same stimulus condition (**Supplementary Fig. S4**).

Sensory stimulus in fMRI experiments consisted of air puffs delivered at 3-5 Hz to the whisker pad contralateral to the cranial window for a total duration of 20 s (“blocked” design) or 2 s (“event-related” design). **Figure 4** shows an example BOLD response in a fully awake mouse. As for the OG stimulus, BOLD signal change in response to both stimulus conditions localized to the cortical region within the window (**Fig. 4A,D**), and an increase in the BOLD signal was visible for both stimulus conditions in trial-averaged time-courses (**Fig. 4B,E**). Statistically significant activation was detected for the blocked design (**Fig. 4C**). As with 2-photon imaging, we rejected stimulus trials with significant motion identified by analysis of the surveillance video (see **Methods** and **Supplementary Movie 1**). When significant motion occurred somewhere within a stimulus trial, we always rejected the entire trial. The proportion of rejected trials was similar to that in 2-photon imaging: ~15-20% and ~5-10% for sensory and OG stimuli, respectively.

In contrast to Figures 3 and 4 where the mouse was fully awake, Figure 5 shows fMRI data acquired under sedation with chlorprothixene. In this case, we observed a larger spread of OG-induced activity, including the contralateral hemisphere (**Fig. 5A**). The highest BOLD response, however, was well mapped to the cortical tissue under the window (**Fig. 5B**). Sedated

animals had lower baseline signal fluctuations, probably explained by reduced neuronal activity and body movement (**Fig. 5C-D** and **Supplementary Fig. S3**). Thus, while not appropriate for quantitative hemodynamic studies (**Supplementary Fig. S2C**), BOLD fMRI in sedated mice may still be useful for troubleshooting the protocol and procedure. This is due to high SNR of the BOLD signal and limited motion artifacts in sedated animals. Also, no trials were rejected due to motion under sedation.

Discussion

In the present study, we have achieved BOLD fMRI in fully awake mice, chronically implanted with optical windows, in response to sensory and OG stimuli. Compared to our published data from rats anesthetized with α -chloralose (25), the BOLD signal induced by sensory stimulation in awake mice was ~3 times smaller when normalized by the corresponding averaged arteriolar dilation (awake mice in the present study: ~0.5% BOLD, ~7% dilation; anesthetized rats in Tian et al. (2010): ~2% BOLD, ~10% dilation). This difference can be caused by slower baseline blood flow under anesthesia leading to an increase in the fraction of O_2 extracted from blood by tissue. Hypothetically, if the baseline neuronal activity and cerebral metabolic rate of O_2 ($CMRO_2$) remain the same, slower flow would lead to a higher O_2 extraction fraction resulting in higher amount of HbR in the voxel and lower baseline level of the BOLD signal. Thus, we speculate that if α -chloralose anesthesia affects the baseline blood flow more than it affects neuronal activity and neurovascular coupling, the stimulus may produce a greater Δ BOLD signal between the baseline and stimulated conditions. An alternative explanation for the low BOLD response in response to sensory stimulation in the present study may be due to reduced attention of the animals to the stimulus during BOLD fMRI acquisition. Our animals were well trained and habituated to the noise of an echo planar imaging (EPI) pulse sequence used for BOLD acquisition, head fixation and LED lighting, as well as to wearing protective ear plugs (see **Methods**). However, we cannot rule out that some environmental factors, e.g., a

residual vibration transmitted through the air cushions, distracted the animals' attention to the air puff.

In conclusion, the present study provides a proof-of-principle demonstration for using chronic optical cranial windows in animal BOLD fMRI studies. These windows support multimodal optical imaging, from detailed 2-photon microscopy throughout the cortical depth and beyond to meso- and macroscopic optical imaging using all available optical contrasts mechanisms. We demonstrate that the presence of the window results in minimal losses of the BOLD fMRI signal while allowing OG stimulation by simply positioning an optical fiber next to the window. These windows are stable and support longitudinal imaging alternating between imaging modalities for each subject over weeks and months. In the future, sampling multiple physiological parameters in an awake behaving mouse across scales and measurement modalities, including BOLD fMRI, will be instrumental for bridging BOLD fMRI signals, induced by a complex behavior, to the underlying activity of neuronal circuits. The ability to perform longitudinal studies, while alternating between imaging modalities and manipulating neuronal activity with OG tools, can also facilitate neurophysiological underpinning of spontaneous ("resting state") hemodynamic fluctuations (49-52) as well as cortical MRI signals in response to clinically-relevant perturbations of brain activity (53).

Figure Legends

Figure 1. MRI-compatible headpost assembly and image quality across modalities

- A. Schematics of the borosilicate glass window implant.
- B. Schematic illustration of the window implant over the whisker representation within the primary somatosensory cortex (SI) and the headpost fixed to the skull overlaying the other (contralateral) hemisphere.
- C. Images of the brain vasculature through the glass window implant obtained by 2-photon imaging of fluorescein isothiocyanate (FITC)-labeled dextran injected intravenously. The images illustrate preserved integrity of the vasculature between days 1 (top) and 28 (bottom) following surgical implantation.
- D) Two-photon image stack obtained with Alexa 680 labeled dextran injected intravenously illustrating the capability of deep imaging.
- E) Corrected GE EPI image (left) and a corresponding structural image (TurboRARE, right). Red arrows point to the peripheral edges of the implant, i.e., the glass/bone boundary. The red line indicates the bottom of the glass implant, i.e., the glass/brain boundary.

Figure 2. From 2-photon microscopy to mesoscopic OIS/LS imaging providing a proxy for the BOLD signal

- A. Image of the surface vasculature calculated as a maximum intensity projection (MIP) of an image stack 0–300 μm in depth using a 4x objective. Individual images were acquired every 10 μm .
- B. A zoomed-in view of the region within the red square in (A) acquired with a 20x objective.
- C. Top left: A plane 250 μm below the surface corresponding to the region outlined in blue in (B). The yellow circle indicates a small diving arteriole. Top right: An example temporal diameter change profile acquired from the arteriole outlined by the yellow circle imaged 250 μm below the

surface. The vessel diameter was captured by repeated line-scans across the vessel. These line-scans form a space-time image when stacked sequentially, from left to right. White arrowheads indicate the onset of stimulus trials (air puffs to the whisker pad); four trials are shown. Bottom: Single-vessel dilation time-courses extracted from data such as that illustrated in (C). Time-courses for individual trials are overlaid for OG stimulus (left, n=19 trials) and sensory stimulus (right, n=160 trials); the thick lines show the average. The stimulus onset is indicated by the blue vertical line and a black arrowhead for the OG and sensory panels, respectively.

D. Concurrent OIS and LS contrast imaging in the same subject as in (A)-(C). Left: A CCD reflectance image of the surface vasculature. Middle: The corresponding LS contrast image. Right: Ratio images of HbO (extracted from the OIS data, see **Methods**) and LS contrast showing the region of activation following OG stimulation. The location of optical fiber is indicated on all images (black dotted line). The same arteriole as in (C) is outlined by yellow circles. The black parallelogram indicates the region of interest (ROI) used for extraction of time-courses in (E).

E. Time-courses of HbO and HbR (shown in red and blue, respectively) and LS contrast (shown in black) in response to OG and sensory stimulation. These time-courses were extracted from the polygonal ROI shown in (D).

Figure 3. The BOLD signal in response to OG stimuli in a fully awake mouse

A. Spatiotemporal evolution of the BOLD signal change from a single slice cutting through the center of the evoked response, presented as trial-averaged ratio maps, in response to a 20-s train of 100-ms light pulses delivered at 1 Hz (“blocked” OG stimulus) in a single *Emx1-Cre/Ai32* subject. EPI images were thresholded to reflect the sensitivity of the surface RF coil (for display purposes only). The ratio images are overlaid on the structural (TurboRARE) image of the same slice.

B. BOLD response time-courses extracted from the active ROI. 28 stimulus trials are superimposed. The average is overlaid in thick black. For the full range of the y-axis, see **Supplementary Fig. S3**.

C. Thresholded ($p = 0.001$ uncorrected) statistical p-map corresponding to the data shown in (A) assuming the standard hemodynamic response function (HRF) with temporal derivatives (see **Methods**). This map was used to define the ROI for extraction of time-courses in (B) and (E).

D. As in (A) for single 100-ms light pulses (“event-related” OG stimulus) in the same subject.

E. BOLD response time-courses corresponding to (D). 69 stimulus trials are superimposed. The average is overlaid in thick black.

Figure 4. The BOLD signal in response to sensory stimuli in a fully awake mouse

Conventions are the same as in **Fig. 3**. (A)-(C) correspond to 20-s stimulus duration ($n=21$ trials). (D)-(E) correspond to 2-s stimulus duration ($n=57$ trials). For the full range of the y-axis for the BOLD signal time-courses, see **Supplementary Fig. S3**.

Figure 5. The BOLD signal under sedation with chlorprothixene

A. Spatiotemporal evolution of the BOLD signal change from a single slice cutting through the center of the evoked response, presented as ratio maps, in response to single 100-ms light pulses in a sedated Emx1-Cre/Ai32 subject.

B. Corresponding time-resolved p-maps. In this case, we made no assumptions about the shape of the HRF (i.e. using a “finite impulse response” model).

C. The BOLD signal time-course from the active ROI (defined by thresholding of the p-value map). Black arrowheads indicate onset on stimulation trials.

D. Superimposed BOLD response time-courses for 72 stimulus trials. The average is overlaid in thick black.

Acknowledgments

We gratefully acknowledge support from the NIH (MH111359, NS057198, U01NS094232, and S10RR029050). M. Desjardins was supported by a postdoctoral scholarship from the Natural Sciences and Engineering Research Council of Canada. K. Kılıç was supported by a postdoctoral fellowship from the International Headache Society and TUBITAK. M. Thunemann was supported by a postdoctoral fellowship from the German Research Council (DFG TH 2031/1).

Financial Disclosure

The authors report no biomedical financial interests or potential conflicts of interest.

References

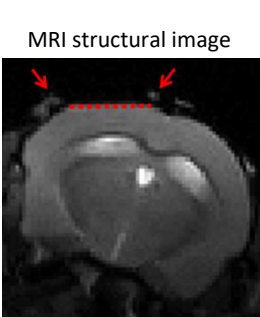
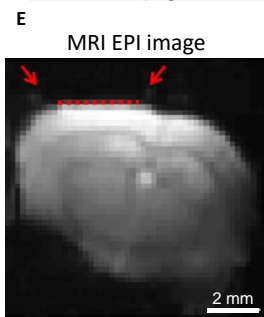
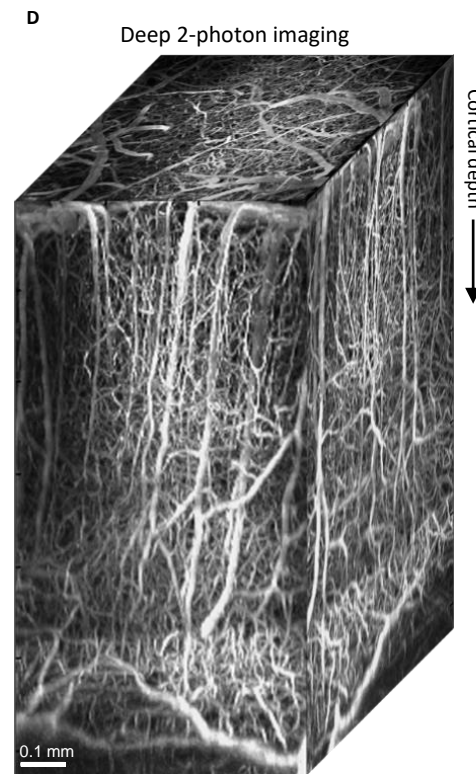
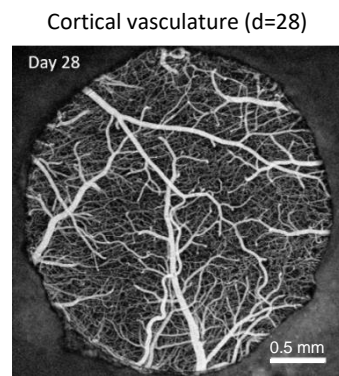
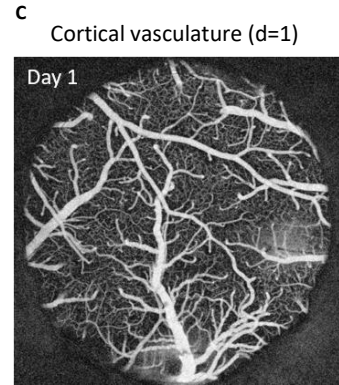
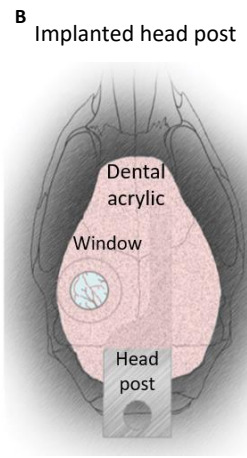
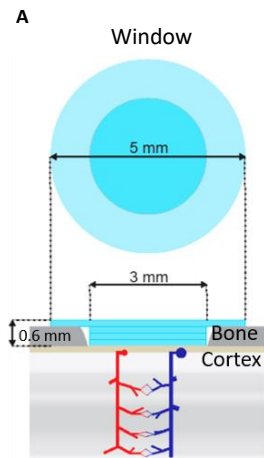
1. Uhlirova H, Kilic K, Tian P, Sakadzic S, Gagnon L, Thunemann M, et al. (2016): The roadmap for estimation of cell-type-specific neuronal activity from non-invasive measurements. *Philos Trans R Soc Lond B Biol Sci.* 371.
2. Gagnon L, Sakadzic S, Lesage F, Musacchia JJ, Lefebvre J, Fang Q, et al. (2015): Quantifying the microvascular origin of BOLD-fMRI from first principles with two-photon microscopy and an oxygen-sensitive nanoprobe. *J Neurosci.* 35:3663-3675.
3. Gagnon L, Smith AF, Boas DA, Devor A, Secomb TW, Sakadzic S (2016): Modeling of Cerebral Oxygen Transport Based on In vivo Microscopic Imaging of Microvascular Network Structure, Blood Flow, and Oxygenation. *Front Comput Neurosci.* 10:82.
4. Fang Q, Sakadzic S, Ruvinskaya L, Devor A, Dale AM, Boas DA (2008): Oxygen advection and diffusion in a three-dimensional vascular anatomical network. *Opt Express.* 16:17530-17541.
5. Boas DA, Jones SR, Devor A, Huppert TJ, Dale AM (2008): A vascular anatomical network model of the spatio-temporal response to brain activation. *Neuroimage.* 40:1116-1129.
6. Gagnon L, Sakadzic S, Lesage F, Pouliot P, Dale AM, Devor A, et al. (2016): Validation and optimization of hypercapnic-calibrated fMRI from oxygen-sensitive two-photon microscopy. *Philos Trans R Soc Lond B Biol Sci.* 371.
7. Deisseroth K (2015): Optogenetics: 10 years of microbial opsins in neuroscience. *Nat Neurosci.* 18:1213-1225.
8. Makino H, Komiyama T (2015): Learning enhances the relative impact of top-down processing in the visual cortex. *Nat Neurosci.* 18:1116-1122.
9. Ferris CF, Yee JR, Kenkel WM, Dumais KM, Moore K, Veenema AH, et al. (2015): Distinct BOLD Activation Profiles Following Central and Peripheral Oxytocin Administration in Awake Rats. *Front Behav Neurosci.* 9:245.
10. Chang PC, Procissi D, Bao Q, Centeno MV, Baria A, Apkarian AV (2016): Novel method for functional brain imaging in awake minimally restrained rats. *J Neurophysiol.* 116:61-80.
11. Yee JR, Kenkel W, Caccaviello JC, Gamber K, Simmons P, Nedelman M, et al. (2015): Identifying the integrated neural networks involved in capsaicin-induced pain using fMRI in awake TRPV1 knockout and wild-type rats. *Front Syst Neurosci.* 9:15.
12. Ferris CF, Kulkarni P, Toddes S, Yee J, Kenkel W, Nedelman M (2014): Studies on the Q175 Knock-in Model of Huntington's Disease Using Functional Imaging in Awake Mice: Evidence of Olfactory Dysfunction. *Front Neurol.* 5:94.
13. Harris AP, Lennen RJ, Marshall I, Jansen MA, Pernet CR, Brydges NM, et al. (2015): Imaging learned fear circuitry in awake mice using fMRI. *Eur J Neurosci.* 42:2125-2134.
14. Lee JH, Durand R, Gradinaru V, Zhang F, Goshen I, Kim DS, et al. (2010): Global and local fMRI signals driven by neurons defined optogenetically by type and wiring. *Nature.* 465:788-792.
15. Kolodziej A, Lippert M, Angenstein F, Neubert J, Pethe A, Grosser OS, et al. (2014): SPECT-imaging of activity-dependent changes in regional cerebral blood flow induced by electrical and optogenetic self-stimulation in mice. *Neuroimage.* 103:171-180.
16. Liang Z, Watson GD, Alloway KD, Lee G, Neuberger T, Zhang N (2015): Mapping the functional network of medial prefrontal cortex by combining optogenetics and fMRI in awake rats. *Neuroimage.* 117:114-123.
17. Aksenov DP, Li L, Miller MJ, Wyrwicz AM (2016): Blood oxygenation level dependent signal and neuronal adaptation to optogenetic and sensory stimulation in somatosensory cortex in awake animals. *Eur J Neurosci.* 44:2722-2729.

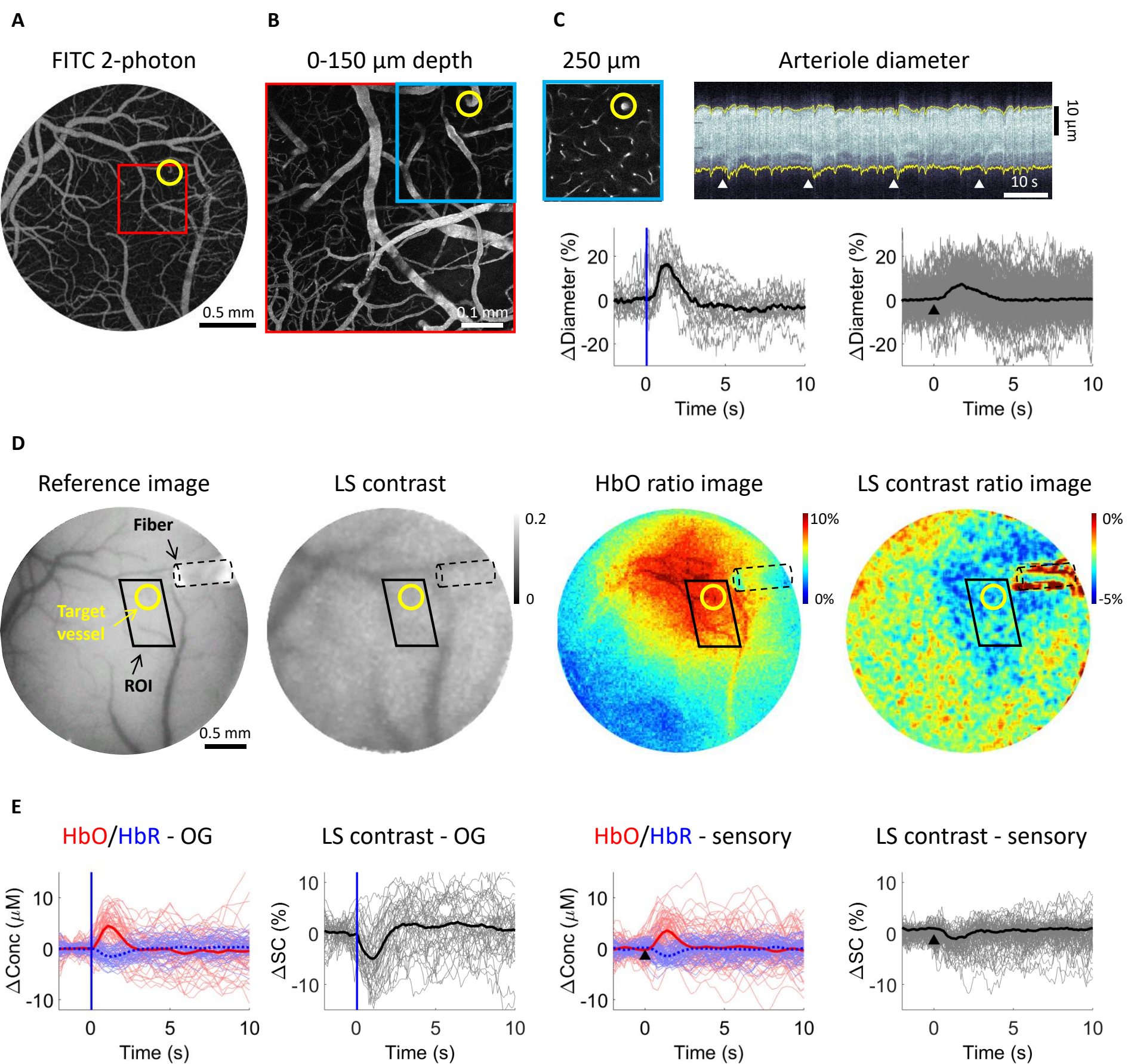
18. Brocka M, Helbing C, Vincenz D, Scherf T, Montag D, Goldschmidt J, et al. (2018): Contributions of dopaminergic and non-dopaminergic neurons to VTA-stimulation induced neurovascular responses in brain reward circuits. *Neuroimage*. 177:88-97.
19. Desai M, Kahn I, Knoblich U, Bernstein J, Atallah H, Yang A, et al. (2011): Mapping brain networks in awake mice using combined optical neural control and fMRI. *J Neurophysiol*. 105:1393-1405.
20. Uhlirova H, Kilic K, Tian P, Thunemann M, Desjardins M, Saisan PA, et al. (2016): Cell type specificity of neurovascular coupling in cerebral cortex. *Elife*. 5.
21. Goldey GJ, Roumis DK, Glickfeld LL, Kerlin AM, Reid RC, Bonin V, et al. (2014): Removable cranial windows for long-term imaging in awake mice. *Nat Protoc*. 9:2515-2538.
22. Holland D, Kuperman JM, Dale AM (2010): Efficient correction of inhomogeneous static magnetic field-induced distortion in Echo Planar Imaging. *Neuroimage*. 50:175-183.
23. Wapler MC, Leupold J, Dragonu I, von Elverfeld D, Zaitsev M, Wallrabe U (2014): Magnetic properties of materials for MR engineering, micro-MR and beyond. *J Magn Reson*. 242:233-242.
24. Nizar K, Uhlirova H, Tian P, Saisan PA, Cheng Q, Reznichenko L, et al. (2013): In vivo stimulus-induced vasodilation occurs without IP3 receptor activation and may precede astrocytic calcium increase. *J Neurosci*. 33:8411-8422.
25. Tian P, Teng IC, May LD, Kurz R, Lu K, Scadeng M, et al. (2010): Cortical depth-specific microvascular dilation underlies laminar differences in blood oxygenation level-dependent functional MRI signal. *Proc Natl Acad Sci U S A*. 107:15246-15251.
26. Zhao S, Ting JT, Atallah HE, Qiu L, Tan J, Gloss B, et al. (2011): Cell type-specific channelrhodopsin-2 transgenic mice for optogenetic dissection of neural circuitry function. *Nat Methods*. 8:745-752.
27. Bonder DE, McCarthy KD (2014): Astrocytic Gq-GPCR-linked IP3R-dependent Ca²⁺ signaling does not mediate neurovascular coupling in mouse visual cortex in vivo. *J Neurosci*. 34:13139-13150.
28. Monai H, Ohkura M, Tanaka M, Oe Y, Konno A, Hirai H, et al. (2016): Calcium imaging reveals glial involvement in transcranial direct current stimulation-induced plasticity in mouse brain. *Nat Commun*. 7:11100.
29. Otsu Y, Couchman K, Lyons DG, Collot M, Agarwal A, Mallet JM, et al. (2015): Calcium dynamics in astrocyte processes during neurovascular coupling. *Nat Neurosci*. 18:210-218.
30. Devor A, Sakadzic S, Saisan PA, Yaseen MA, Roussakis E, Srinivasan VJ, et al. (2011): "Overshoot" of O₂ is required to maintain baseline tissue oxygenation at locations distal to blood vessels. *J Neurosci*. 31:13676-13681.
31. Sakadzic S, Roussakis E, Yaseen MA, Mandeville ET, Srinivasan VJ, Arai K, et al. (2010): Two-photon high-resolution measurement of partial pressure of oxygen in cerebral vasculature and tissue. *Nat Methods*. 7:755-759.
32. Lecoq J, Parpaleix A, Roussakis E, Ducros M, Goulam Houssen Y, Vinogradov SA, et al. (2011): Simultaneous two-photon imaging of oxygen and blood flow in deep cerebral vessels. *Nat Med*. 17:893-898.
33. Lyons DG, Parpaleix A, Roche M, Charpak S (2016): Mapping oxygen concentration in the awake mouse brain. *Elife*. 5.
34. Parpaleix A, Goulam Houssen Y, Charpak S (2013): Imaging local neuronal activity by monitoring PO₂ transients in capillaries. *Nat Med*. 19:241-246.
35. Sakadzic S, Yaseen MA, Jaswal R, Roussakis E, Dale AM, Buxton RB, et al. (2016): Two-photon microscopy measurement of cerebral metabolic rate of oxygen using periarteriolar oxygen concentration gradients. *Neurophotonics*. 3:045005.
36. Machler P, Wyss MT, Elsayed M, Stobart J, Gutierrez R, von Faber-Castell A, et al. (2016): In Vivo Evidence for a Lactate Gradient from Astrocytes to Neurons. *Cell Metab*. 23:94-102.

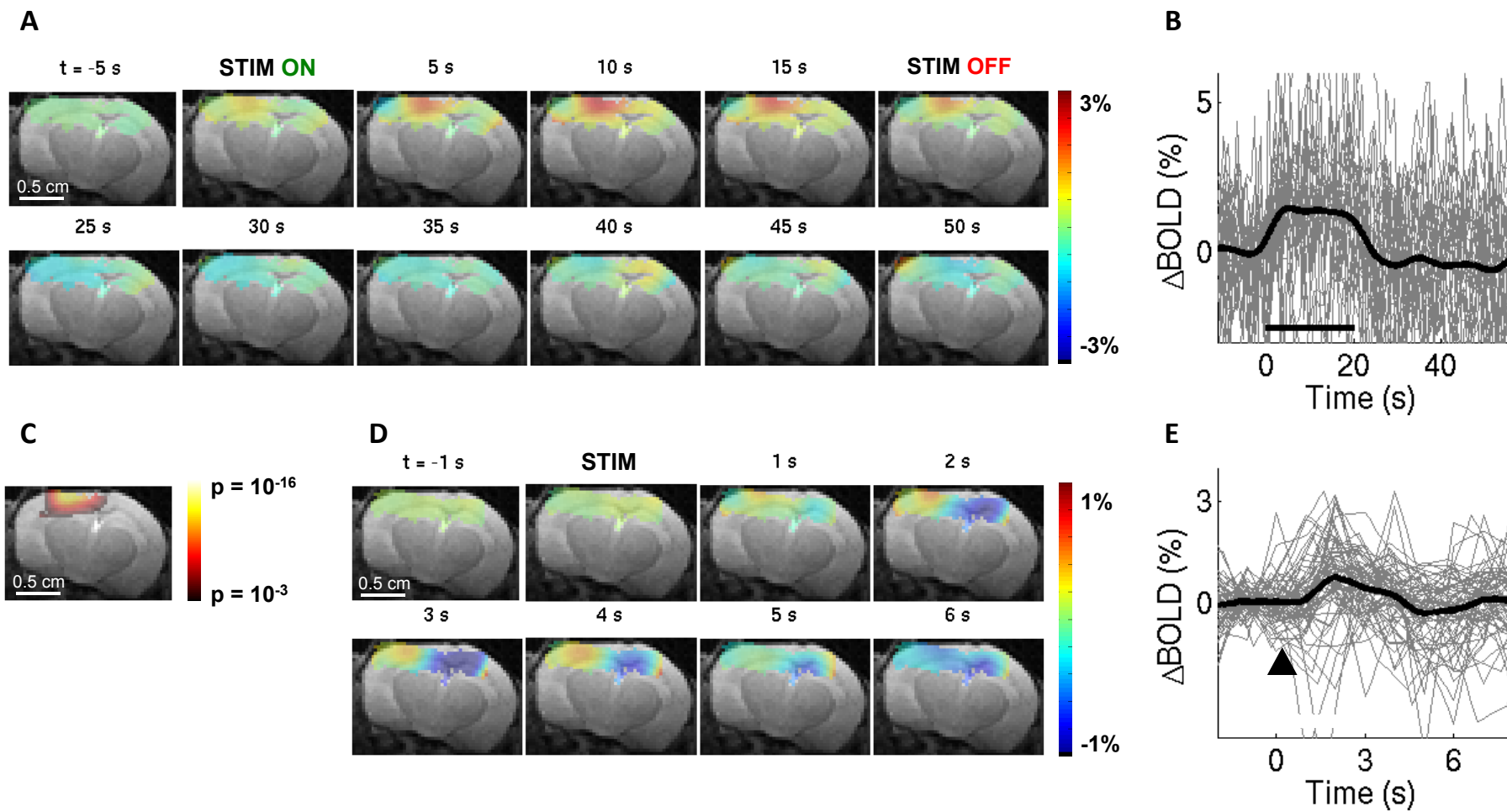
37. Devor A, Sakadzic S, Yaseen MA, Roussakis E, Tian P, Slovín H, et al. (2013): Functional imaging of cerebral oxygenation with intrinsic optical contrast and phosphorescent probes. In: Weber B, Helmchen F, editors. *Optical imaging of cortical circuit dynamics*. New York: Springer.
38. Dunn AK, Devor A, Bolay H, Andermann ML, Moskowitz MA, Dale AM, et al. (2003): Simultaneous imaging of total cerebral hemoglobin concentration, oxygenation, and blood flow during functional activation. *Opt Lett*. 28:28-30.
39. Dunn AK, Devor A, Dale AM, Boas DA (2005): Spatial extent of oxygen metabolism and hemodynamic changes during functional activation of the rat somatosensory cortex. *Neuroimage*. 27:279-290.
40. Christie IN, Wells JA, Southern P, Marina N, Kasparov S, Gourine AV, et al. (2013): fMRI response to blue light delivery in the naive brain: implications for combined optogenetic fMRI studies. *Neuroimage*. 66:634-641.
41. Rungta RL, Osmanski BF, Boido D, Tanter M, Charpak S (2017): Light controls cerebral blood flow in naive animals. *Nat Commun*. 8:14191.
42. Devor A, Dunn AK, Andermann ML, Ulbert I, Boas DA, Dale AM (2003): Coupling of total hemoglobin concentration, oxygenation, and neural activity in rat somatosensory cortex. *Neuron*. 39:353-359.
43. Devor A, Ulbert I, Dunn AK, Narayanan SN, Jones SR, Andermann ML, et al. (2005): Coupling of the cortical hemodynamic response to cortical and thalamic neuronal activity. *Proc Natl Acad Sci U S A*. 102:3822-3827.
44. Grinvald A, Sharon D, Omer D, Vanzetta I (2016): Imaging the Neocortex Functional Architecture Using Multiple Intrinsic Signals: Implications for Hemodynamic-Based Functional Imaging. *Cold Spring Harb Protoc*. 2016:pdb top089375.
45. Jones M, Berwick J, Johnston D, Mayhew J (2001): Concurrent optical imaging spectroscopy and laser-Doppler flowmetry: the relationship between blood flow, oxygenation, and volume in rodent barrel cortex. *Neuroimage*. 13:1002-1015.
46. Devor A, Boas D, Einevoll GT, Buxton RB, Dale AM (2012): Neuronal Basis of Non-Invasive Functional Imaging: From Microscopic Neurovascular Dynamics to BOLD fMRI. In: In-Young Choi RG, editor. *Neural Metabolism In Vivo*. New York: Springer.
47. Gorski JA, Talley T, Qiu M, Puelles L, Rubenstein JL, Jones KR (2002): Cortical excitatory neurons and glia, but not GABAergic neurons, are produced in the Emx1-expressing lineage. *J Neurosci*. 22:6309-6314.
48. Madisen L, Mao T, Koch H, Zhuo JM, Berenyi A, Fujisawa S, et al. (2012): A toolbox of Cre-dependent optogenetic transgenic mice for light-induced activation and silencing. *Nat Neurosci*. 15:793-802.
49. Ma Y, Shaik MA, Kozberg MG, Kim SH, Portes JP, Timerman D, et al. (2016): Resting-state hemodynamics are spatiotemporally coupled to synchronized and symmetric neural activity in excitatory neurons. *Proc Natl Acad Sci U S A*. 113:E8463-E8471.
50. Mateo C, Knutsen PM, Tsai PS, Shih AY, Kleinfeld D (2017): Entrainment of Arteriole Vasomotor Fluctuations by Neural Activity Is a Basis of Blood-Oxygenation-Level-Dependent "Resting-State" Connectivity. *Neuron*. 96:936-948 e933.
51. Murphy MC, Chan KC, Kim SG, Vazquez AL (2018): Macroscale variation in resting-state neuronal activity and connectivity assessed by simultaneous calcium imaging, hemodynamic imaging and electrophysiology. *Neuroimage*. 169:352-362.
52. Schwalm M, Schmid F, Wachsmuth L, Backhaus H, Kronfeld A, Aedo Jury F, et al. (2017): Cortex-wide BOLD fMRI activity reflects locally-recorded slow oscillation-associated calcium waves. *Elife*. 6.

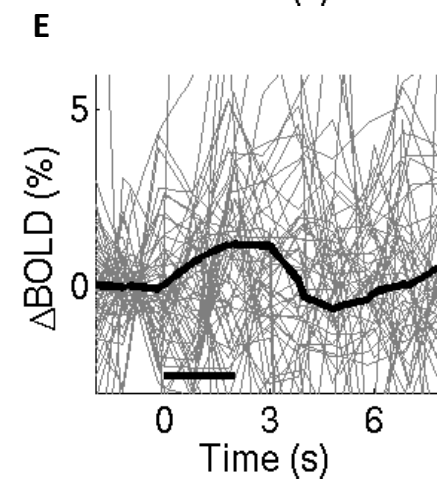
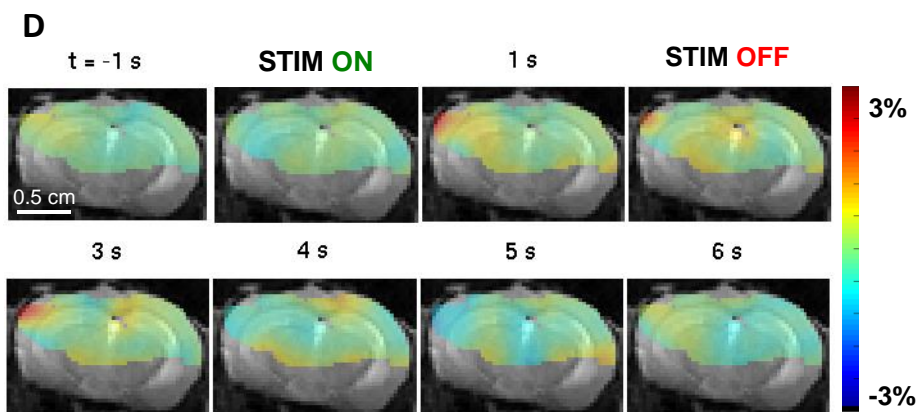
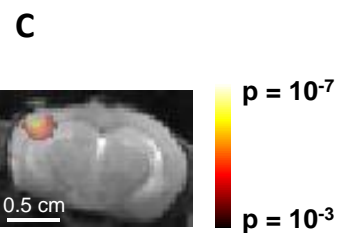
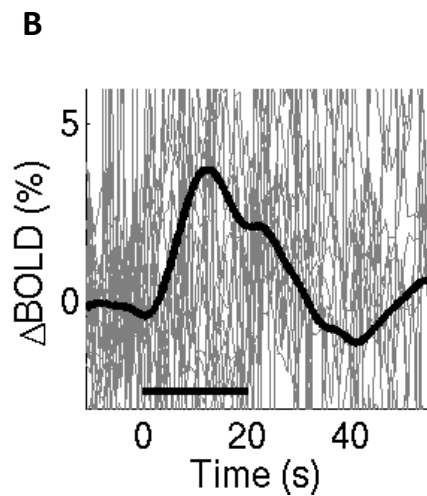
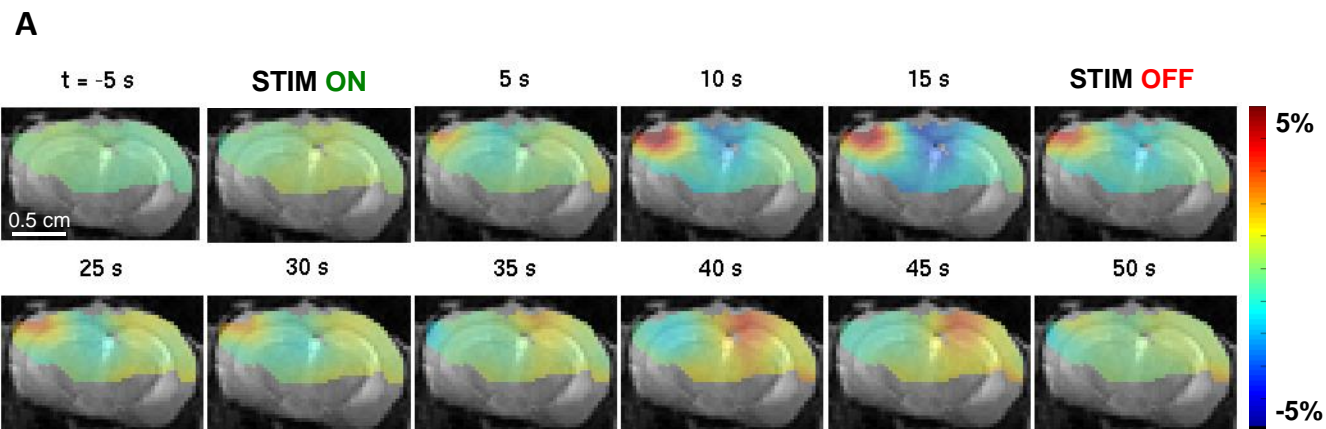
53. Albaugh DL, Salzwedel A, Van Den Berge N, Gao W, Stuber GD, Shih YY (2016): Functional Magnetic Resonance Imaging of Electrical and Optogenetic Deep Brain Stimulation at the Rat Nucleus Accumbens. *Sci Rep.* 6:31613.

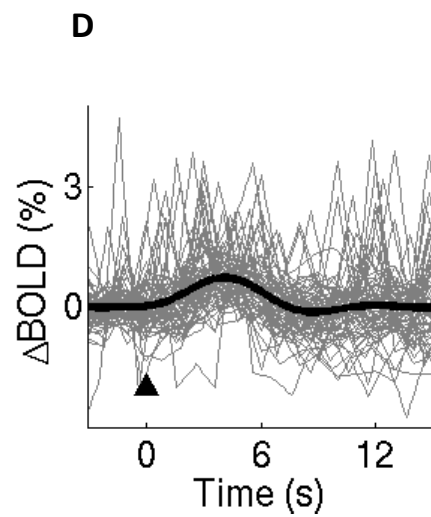
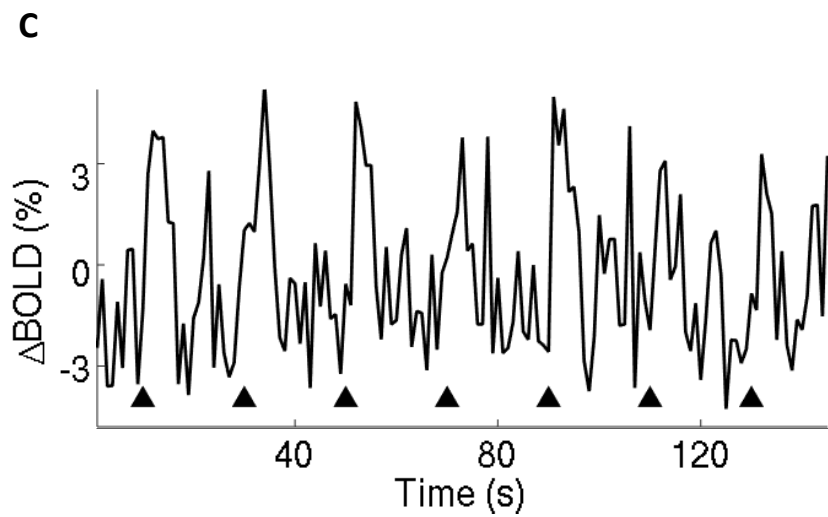
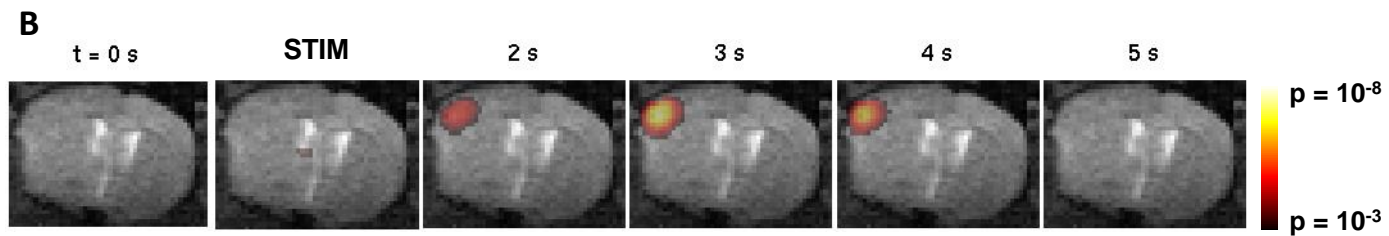
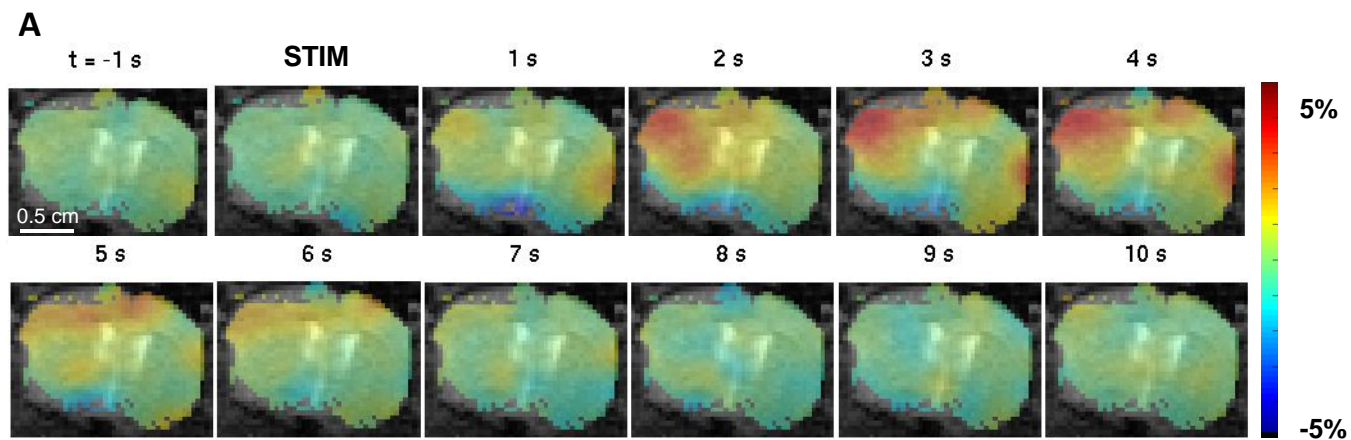
ACCEPTED MANUSCRIPT









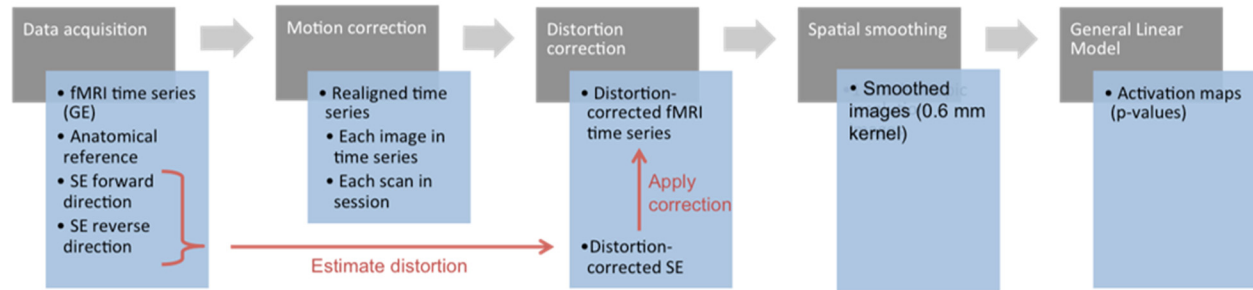


Awake Mouse Imaging: From Two-Photon Microscopy to Blood Oxygenation Level-Dependent Functional Magnetic Resonance Imaging

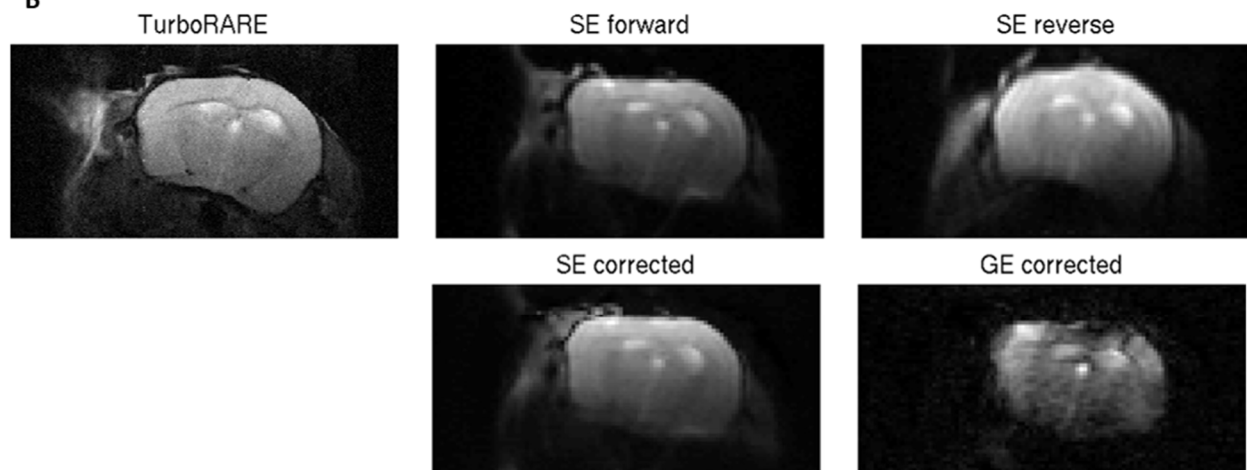
Supplemental Information

Supplementary Figure S1.

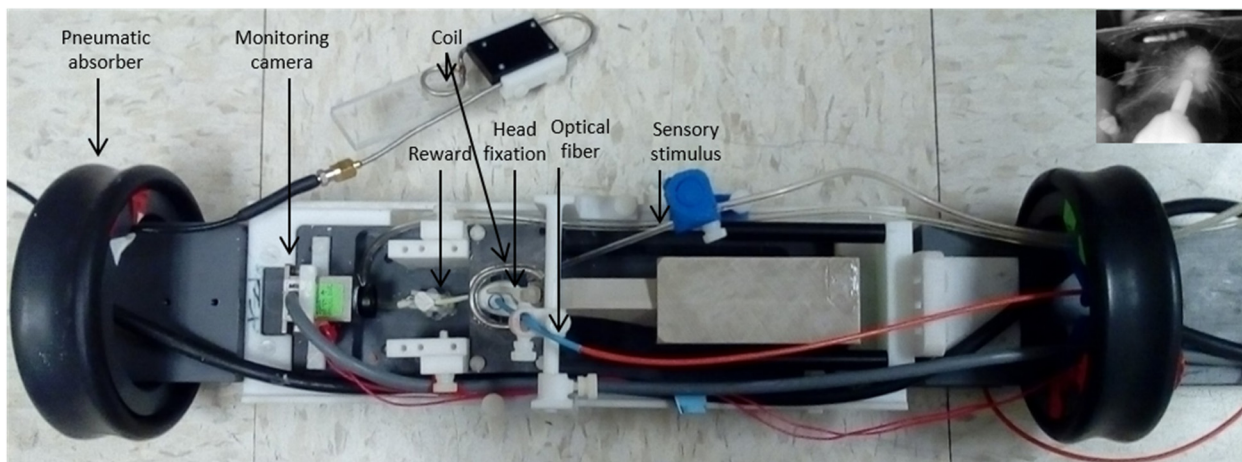
MRI acquisition and correction of EPI image distortion due to B_0 field inhomogeneity



B



C



A. Schematics of the protocol for MRI data acquisition and processing.

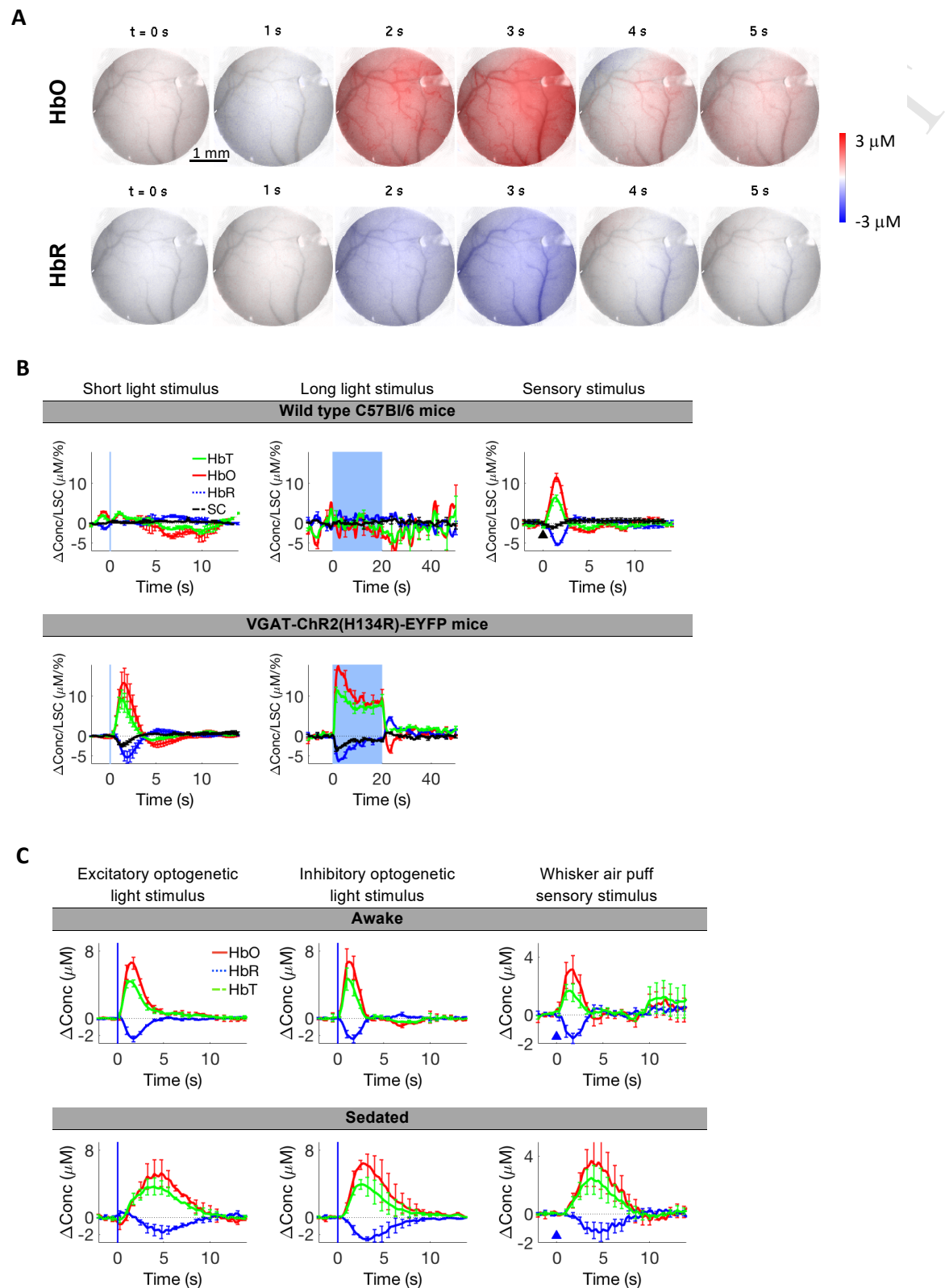
B. Top: The structural image (TurboRARE) and forward and reverse SE EPI scans. Bottom: corrected SE and GE EPI scans. All images were acquired using the same geometry and slice thickness. Matrix size was 100x50 for EPI and 256x256 for TurboRARE, over a 2x1 cm FOV. TurboRARE images were resampled to match EPI resolution to facilitate visual comparison.

C. Custom-made MRI-compatible mouse cradle. Functional components include, from left to right:

- 1) Inflatable pneumatic air chambers to dampen vibration.
- 2) Real time monitoring and recording using a commercial MRI-compatible camera (MRC Systems GmbH). A blue LED played a double role as an illumination source for the camera and as a mask to prevent the mouse visual perception of the blue laser used for OG stimulation.
- 3) A plastic tube used for delivery of the reward, a drop of sweetened condensed milk.
- 4) A homemade RF induction coil.
- 5) A mechanism for head fixation made of PEEK plastic parts.
- 6) An optical fiber (Thorlabs FG200UEA, 200 μm core, 0.22 NA) coupled to a blue laser (OptoEngine LLC 450 nm laser) for delivery of OG stimulation. The distal end of the fiber was positioned ~ 0.5 mm above the glass window within the RF coil loop.
- 7) A 2-mm diameter plastic tube connected to picopump (PV830, WPI) that delivered air puffs to the whisker pad.

Top right corner: an image of the mouse through the monitoring camera. The mouse eyes (for monitoring potential stress), whiskers (for verifying deflection upon sensory stimulation), and reward tube are visible.

Supplementary Figure S2. Hemodynamic response kinetics

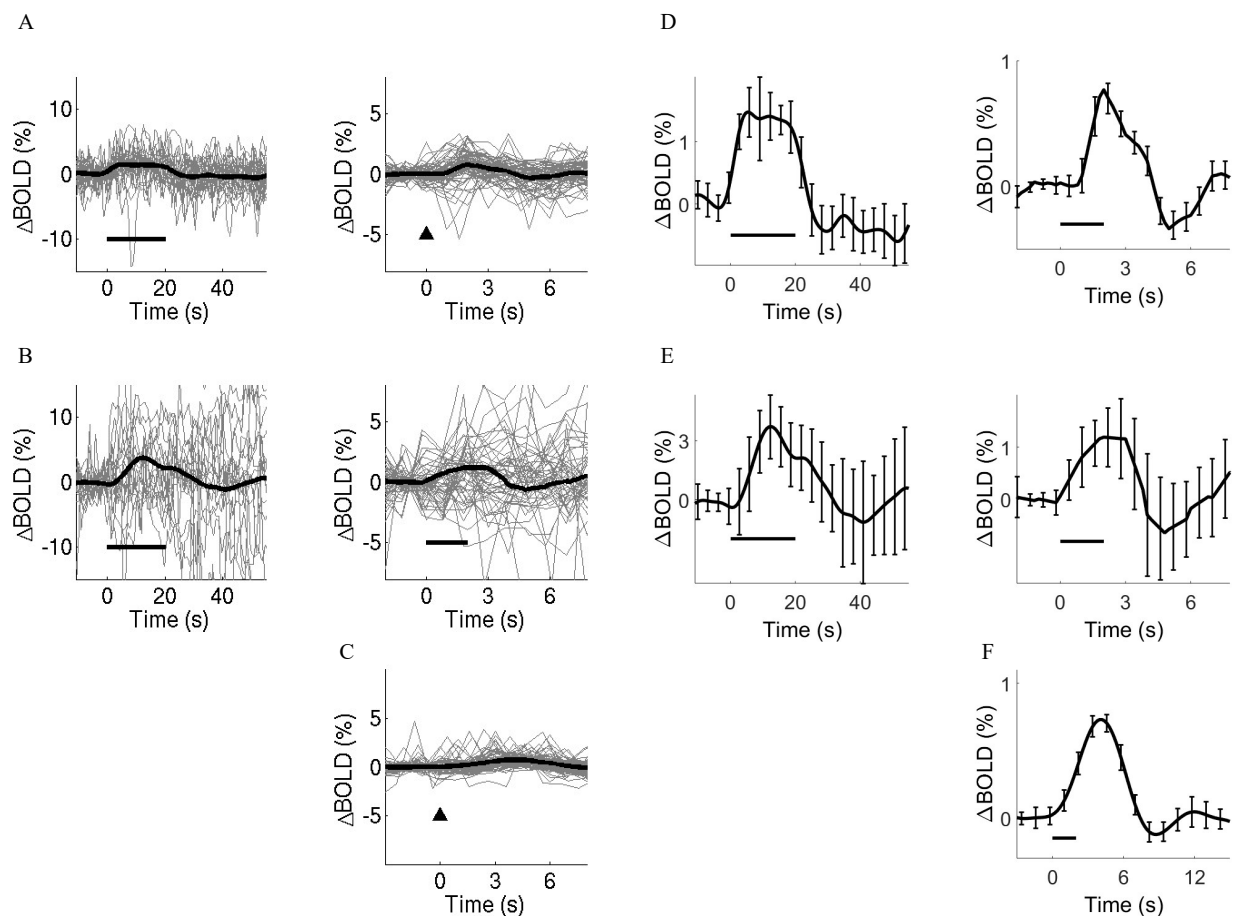


A. Spatiotemporal evolution of OIS signal change in a fully awake mouse (no sedation) corresponding to **Fig. 2D-E**.

B. Control OG experiment in wild type mice. Top: Lack of HbO/HbR response to light stimulation in wild type mice using the same stimulus parameters as in OG experiments (left and middle; $n = 2$ mice, 50 trials per mouse); sensory response measured in the same experimental session as a control. Bottom: typical HbO/HbR responses to light stimulation in VGAT-ChR2(H134R)-EYFP mice ($n = 3$, 100 trials per mouse). The “short” stimulus corresponds to a single 100-ms light pulse. The “long” stimulus corresponds to a 20-s train of 100-ms light pulses delivered at 1 Hz. The error bars indicate standard error between subjects.

C. Effect of sedation. Comparison of the timecourse of HbO/HbR signal in response to OG and sensory stimulation with and without sedation using 1.5 mg/kg chlorprothixene hydrochloride. The error bars indicate standard error between subjects. Three stimulus conditions are shown: 100-ms OG stimulation of pyramidal neurons in *Emx1-Cre/Ai32* mice (left; $n=3$ subjects); 100-ms OG stimulation of inhibitory interneurons in VGAT-ChR2(H134R)-EYFP mice (middle; $n=2$ subjects); sensory stimulation by air puffs to the whiskers (right; $n=5$ subjects).

Supplementary Figure S3.
The BOLD signal time-courses

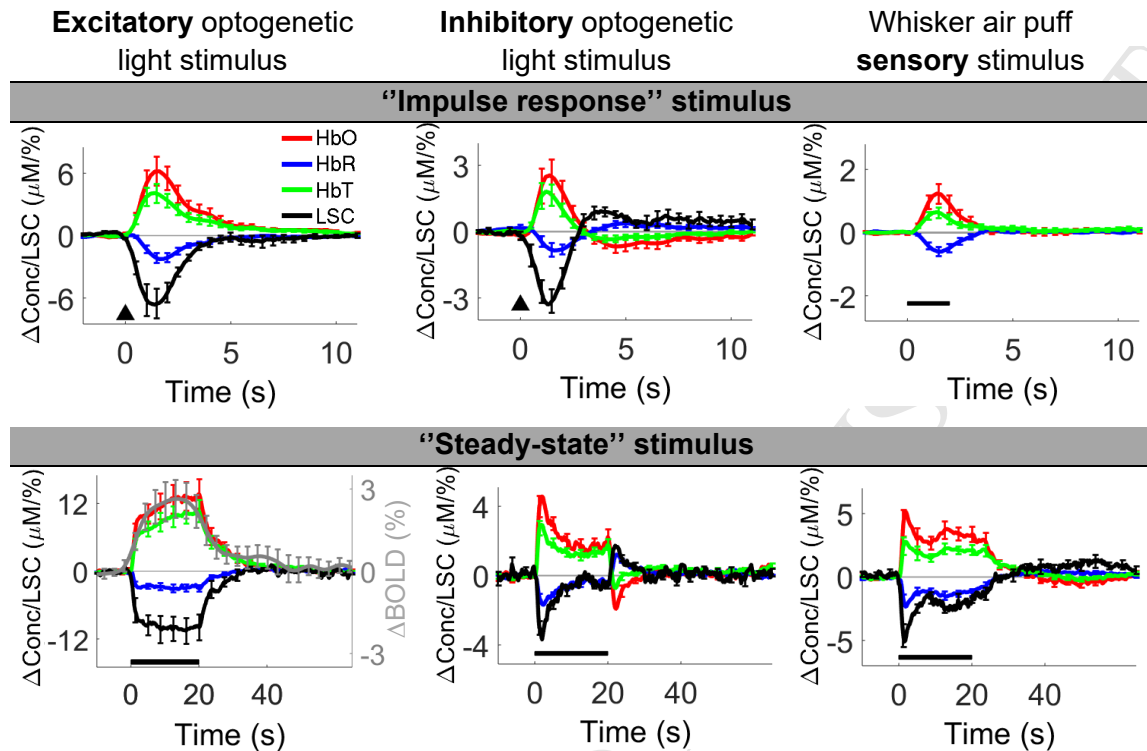


A. BOLD response time-courses from **Figure 3B, E** (awake mouse, OG stimulus). The y-axis limits are chosen to avoid clipping of any individual stimulus trials.

B. As in (A) for **Figure 4B, E** (awake mouse, sensory stimulus).

C. As in (A) for **Figure 5D** (sedated mouse, OG stimulus).

D-F. As (A-C) with error bars showing mean \pm SEM and different y-axis limits.

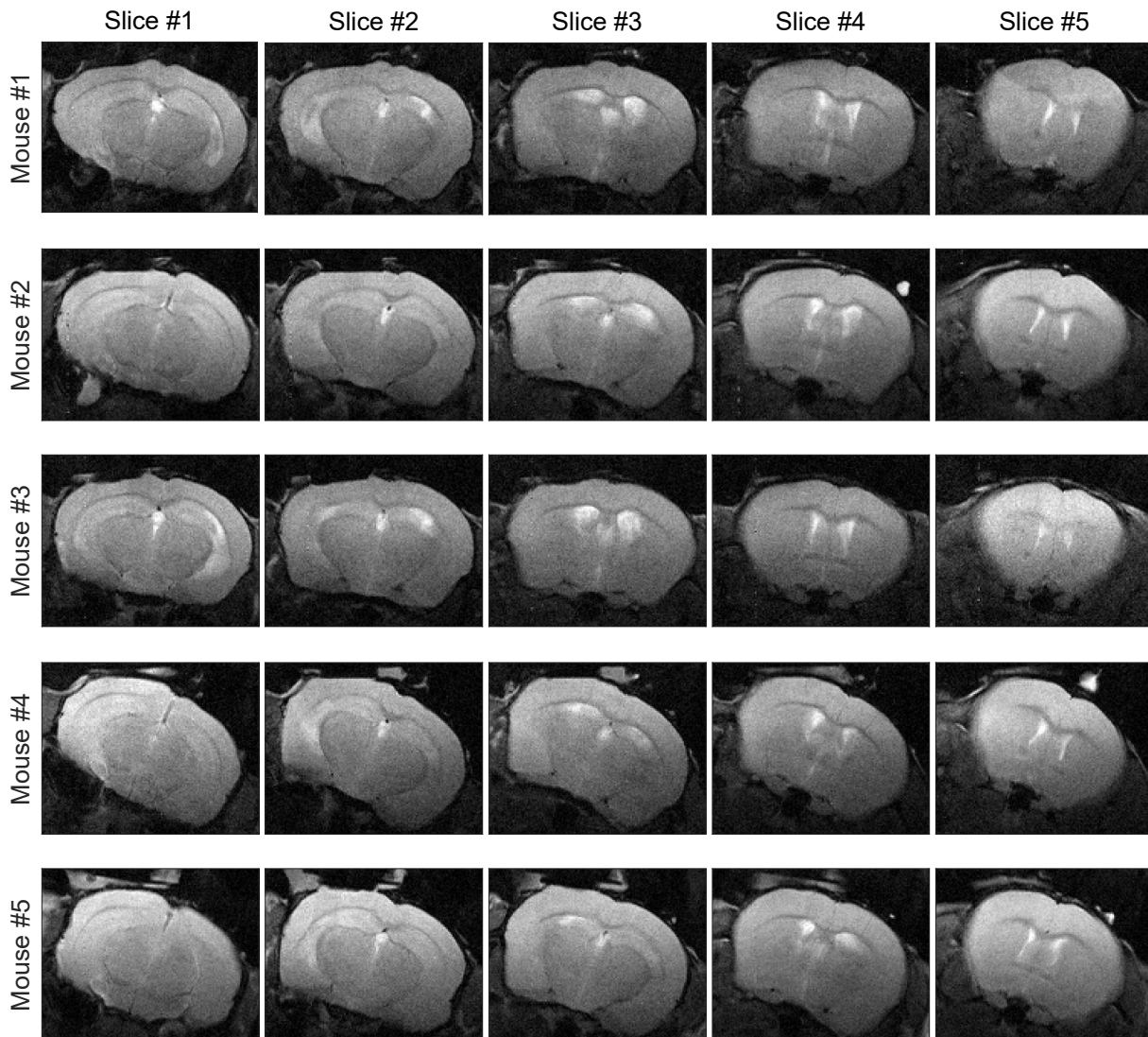
Supplementary Figure S4.**Comparison of the hemodynamic response shape across stimulus conditions**

The figure shows hemodynamic responses, averaged across subjects, as measured by OIS/LS. “Short duration” corresponds to a single 100-ms light pulse. “Long duration” corresponds to a 20-s train of 100-ms pulses delivered at 1 Hz. “Excitatory” and “inhibitory” OG stimuli correspond to OG stimulation in *Emx1-Cre/Ai32* and *VGAT-ChR2(H134R)-EYFP* mice, respectively. Top row: short duration excitatory OG stimulus (left, $n=5$), inhibitory OG stimulus (middle, $n=6$), and sensory stimulus (right, $n=13$). Bottom row: 20-s excitatory OG stimulus (left, $n=5$), inhibitory OG stimulus (middle, $n=9$), and sensory stimulus (right, $n=7$). In addition, the 20-s excitatory OG stimulus includes also BOLD fMRI time-course (gray) obtained from the same 5 subjects under this stimulus condition; the BOLD fMRI scale (gray) is shown to the right.

It can be observed that the 20-s long OG stimulation of excitatory neurons (in *Emx1-Cre/Ai32* mice) produced a hemodynamic response with a plateau for the duration of the stimulus and virtually no post-stimulus undershoot. This behavior is present for both optical and fMRI signals. In contrast, OG stimulation of inhibitory neurons (in *VGAT-ChR2(H134R)-EYFP*) produced an initial overshoot followed by a lower-amplitude plateau and a sharp post-stimulus undershoot. The hemodynamic response to a 20-s long sensory stimulus (a train of air puffs delivered at 3-5 Hz) also had an initial overshoot and a post-stimulus undershoot, although with a smaller amplitude and slower kinetics compared to the *VGAT-ChR2(H134R)-EYFP* case. Some of these differences are also reflected in the responses to short stimuli that can be viewed as the

corresponding “impulse response functions.” As such, response to the short inhibitory OG stimulus has an obvious long-lasting undershoot, which is expected to produce an initial overshoot followed by a low-amplitude plateau and a post-stimulus undershoot when convolved with a 20-s long boxcar.

ACCEPTED MANUSCRIPT

Supplementary Figure S5.**TurboRARE images showing the location of the window**

T2-weighted (TurboRARE) images for each of the 5 MRI slices in 5 representative subjects. Slices 2-3 cut through the optical window as can be seen from the lack of the overlaying bone and slight flattening of the cortex. The location of the window can also be recognized by dental acrylic along the circumference of the window looking bright on the image. These images were acquired using the same geometry as the corresponding EPI slices.

Supplementary Movie S1.**The effect of mouse motion on the EPI images and the effect of the motion correction procedure**

(See separate supplemental file for movie.)

Left: a webcam video of the awake mouse during the fMRI scan. Middle: raw (uncorrected) EPI images. Right: realigned (motion corrected) EPI images. All panels are temporally synchronised. The uncorrected image (the middle panel) visibly jumps up and down during epochs of mouse motion, while the corrected image (on the right) remains stationary.

ACCEPTED MANUSCRIPT

Supplementary Methods

Some of the procedures were similar to those described in our previous study (1).

Animal Procedures

All experimental procedures were performed in accordance with the guidelines established by the UCSD Institutional Animal Care and Use Committee (IACUC). We used 16 adult (age > 8 weeks) mice of either sex including 2 non-transgenic C57BL/6J mice, 9 heterozygous (het) VGAT-ChR2(H134R)-EYFP mice (2) (JAX 014548) and 5 Emx1-Cre/Ai32 double transgenic (het/het) mice (3, 4) (JAX 005628 and 024109). Transgenic animals were on C57BL/6 background.

Implantation of the cranial window and headpost

The surgical procedure was modified from that previously described by the Anderman lab (5). Dexamethasone was injected ~4 h prior to surgery (IP 4.8 mg/kg at 4 mg/ml concentration) to prevent brain swelling due to surgical intervention. All surgical procedures in mice expressing ChR2 were performed in a dark room using a 515 nm longpass filter (Semrock FF01-515/LP-25) in the surgical microscope light source to avoid OG stimulation during installation of the cortical window. Mice were anesthetized with isoflurane during surgical procedures (2% in O₂ initially, 1% in O₂ during all procedures); their body temperature was maintained at 37°C.

The cranial window was implanted over the left Barrel cortex, and the headpost was mounted over the other (right) hemisphere (**Fig. 1B**). Under isoflurane anesthesia, the mouse was secured in a stereotaxic frame (Kopf). Hair was removed with depilatory cream, lidocaine cream (4%) was applied to the skin on top of the head, and skin was cleaned with a povidone-iodine solution followed by 70% isopropyl alcohol (repeated three times). The skull was exposed bilaterally by cutting away the skin over ~1x1 cm area, the underlying connective tissue cleaned away with cotton tipped applicators, and periosteum removed by scratching the bone along the

dorsal surface of the skull with a scalpel blade. At the end of this procedure, the bone was completely dry and free of any overlying tissues. A crosshatch pattern was carved on the skull with a scalpel blade, sparing the exposure and surroundings, to improve adherence of the headpost assembly. On the side of the window, the masseter muscle was pushed down to allow more space around the glass implant. Then, the skin was repositioned to cover the muscles and reattached using small drops of glue (Loctite 4014) on a wooden stick (e.g. autoclaved toothpick or split cotton-tip applicator). The PEEK headpost, used for immobilization of the head during imaging, was attached with glue (Loctite 401) on the bone contralateral to the glass implant. To standardize the position of the imaging window across subjects, the headpost was lowered onto the bone while mounted onto a stereotactic manipulator ensuring a fixed angle and orientation.

A 3-mm diameter circle with the center coordinates of A-P 2 mm and L-R 3 mm (relative to bregma) was drawn on the bone using a fine marker (Sharpie Permanent Marker) to indicate the target position for the glass implant. Then, the bone along the 3-mm circumference was drilled slowly while cooling with an ice slush made of partially frozen saline. Gelatin sponge (Surgifoam, Ethicon) and Bone Wax (Surgical Specialties Corp.) were used to control bleeding. Eventually, the bone along the drill track was thin enough for a gentle pressure to depress the bone. At that point, the bone was pried away to expose the dural brain surface and replaced with a piece of gelatin sponge soaked in saline (to prevent bleeding and keep the dura moist). Next, the glass implant (**Fig. 1A**) was fit within the exposure, and a stereotaxic manipulator equipped with a plastic pipette tip or a wooden stick was used to gently push onto the glass to make the top and bottom of the implant to rest gently on the bone and dural brain surface, respectively. A drop of agarose (1.5% wt/vol, A9793, Sigma) in saline was applied to fill the space between the bone and the top 5-mm part of the glass implant resting on the bone. The circumference of the 5-mm glass was sealed with dental acrylic (Acrylic Repair Powder and Acrylic Liquid, Henry Schein). Additional dental acrylic was applied around the headpost joining

to the perimeter of the coverslip in order to reinforce the overall assembly. Fluids (5% dextrose) were injected SC before discontinuing anesthesia.

Post-operative analgesia was provided with buprenorphine (0.05 mg/kg SC) injected ~20 min before discontinuation of the anesthesia. A combination of Sulfatrim (antibiotic, 5 ml / 250 ml) and Ibuprofen (NSAID, 20 mg/ml) in drinking water starting one day before the surgery and continuing for five days after the surgery. Generally, full recovery and return to normal behavior are observed within 48 hours post-op.

Behavioral training

Procedures were similar to those described previously (1). Starting at least 7 days after the surgical procedure, mice were habituated in 1 session/day to accept increasingly longer periods of head restraint under the microscope objective or in a mock MRI scanner bore (up to 2 hrs). During the head restraint, the animal was placed on a suspended bed. A drop of sweetened condensed milk was offered every 15-20 min during the fixation as a reward. Habituated head-fixed mice consumed the reward milk. They were free to readjust their body position and from time to time displayed natural grooming behavior. A video camera was used for continuous observation of the mouse during imaging. For optical studies, we used a regular webcam (Lifecam Studio, Microsoft; IR filter removed) with an NIR longpass filter (Midwest Optical LP920-25.5). The IR illumination (M940L3 - IR (940 nm) LED, Thorlabs) was invisible for the PMT photodetectors and generated no imaging artifacts. The camera frames were synchronized with 2-photon imaging and recorded. In fMRI experiments, we used an MR-compatible camera (MRC Systems GmbH). Periods with extensive body movement (e.g., grooming behavior) were excluded during data analysis.

Two-photon imaging

Procedures were similar to those described previously (1). Fluorescein isothiocyanate

(FITC)-labeled dextran (MW = 2 MDa, FD-2000S, Sigma), or Alexa Fluor 680 conjugated to amino-dextran (MW = 2 MDa, Finabio AD2000x100) in-house, was injected IV (50-100 μ l of 5 % (w/v) solution in phosphate-buffered saline) to visualize the vasculature.

Images were obtained using an Ultima two-photon laser scanning microscopy system from Bruker Fluorescence Microscopy (formerly Prairie Technologies) equipped with an Ultra II femtosecond Ti:Sapphire laser (Coherent) tuned between 800-1000 nm. For penetration deeper than \sim 600 μ m, an Optical Parametric Oscillator (Chameleon Compact OPO, Coherent), pumped by the same Ti:Sapphire laser, was tuned to 1280 nm. The OPO was used in conjunction with the intravascular administration of dextran-conjugated Alexa Fluor 680 (6). FITC and Alexa Fluor 680 were imaged using cooled GaAsP detectors (Hamamatsu, H7422P-40).

In experiments involving OG stimulation, the main dichroic mirror contained a 460-480 nm notch (Chroma ZT470/561/NIR TPC). An additional filter blocking wavelengths in the range 458-473 nm (Chroma ZET458-473/561/568/NIR M) was added in front of the PMT block. Nevertheless, residual bleed-through of the 473-nm light prevented us from using GaAsP detectors. Therefore, in these experiments, FITC was imaged using a multi-alkali PMT (Hamamatsu, R3896).

We used a 4x objective (Olympus XLFluor4x/340, NA=0.28) to obtain low-resolution images of the exposure. Olympus 20x (XLUMPlanFLNXW, NA=1.0) water-immersion objective was used for high-resolution imaging. Diameter measurements were performed in a frame-scan mode at 10-20 Hz, or in a “free-hand” line-scan mode with a scan rate of 25-50 Hz. The scan resolution was 0.5 μ m or less.

Spectral and laser speckle imaging of blood oxygenation and flow

Spectral imaging of blood oxygenation was performed simultaneously with laser speckle (LS) imaging of blood flow. Detected light was split via a dichroic mirror, filtered and directed

toward two dedicated detectors for imaging of blood oxygenation and LS contrast, respectively. The filtering was achieved by passing light below 650 nm to the spectral detector, and 780 nm light (FWHM of 10 nm) to the LS detector. Spectral imaging has been described in details previously (7). Briefly, illuminating light from a tungsten-halogen light source (Oriel, Spectra-Physics) was directed through a 6-position rotating filter wheel (560, 570, 580, 590, 600 and 610 nm) coupled to a 12 mm fiber bundle. Images of the 3-mm diameter exposure were acquired by cooled 16 bit CCD camera (Cascade 512B, Photometrics) controlled by Matlab software written in-house. Image acquisitions were triggered at ~18 Hz by individual filters in the filter wheel passing through an optic sensor resulting in temporal resolution of 3 Hz for each color. The spectral data were converted to percent change maps for oxyhemoglobin (HbO) and deoxyhemoglobin (HbR) using the modified Beer-Lambert law. Differential pathlength correction was applied to adjust for the differential optical pathlength through the tissue at different wavelengths. Baseline concentrations of 60 and 40 μM were assumed for HbO and HbR, respectively (8). A laser diode (785 nm, 70 mW) was used as a light source for speckle imaging. Raw speckle images were acquired by a high-speed (~100 Hz) 12-bit CMOS camera (ace acA1920-155um, Basler) controlled by Matlab software written in-house. Speckle contrast was calculated from a series of laser speckle images, acquired with an exposure time of 5 ms and in-plane resolution of ~7 μm , following spatial smoothing using a 7x7 pixel sliding window (9). A decrease in speckle contrast indicated an increase in blood flow (7-9).

Supplementary References

1. Uhlirva H, Kilic K, Tian P, Thunemann M, Desjardins M, Saisan PA, et al. (2016): Cell type specificity of neurovascular coupling in cerebral cortex. *Elife*. 5.
2. Zhao S, Ting JT, Atallah HE, Qiu L, Tan J, Gloss B, et al. (2011): Cell type-specific channelrhodopsin-2 transgenic mice for optogenetic dissection of neural circuitry function. *Nat Methods*. 8:745-752.
3. Gorski JA, Talley T, Qiu M, Puelles L, Rubenstein JL, Jones KR (2002): Cortical excitatory neurons and glia, but not GABAergic neurons, are produced in the Emx1-expressing lineage. *J Neurosci*. 22:6309-6314.
4. Madisen L, Mao T, Koch H, Zhuo JM, Berenyi A, Fujisawa S, et al. (2012): A toolbox of Cre-dependent optogenetic transgenic mice for light-induced activation and silencing. *Nat Neurosci*. 15:793-802.
5. Goldey GJ, Roumis DK, Glickfeld LL, Kerlin AM, Reid RC, Bonin V, et al. (2014): Removable cranial windows for long-term imaging in awake mice. *Nat Protoc*. 9:2515-2538.
6. Kobat D, Durst ME, Nishimura N, Wong AW, Schaffer CB, Xu C (2009): Deep tissue multiphoton microscopy using longer wavelength excitation. *Opt Express*. 17:13354-13364.
7. Dunn AK, Devor A, Bolay H, Andermann ML, Moskowitz MA, Dale AM, et al. (2003): Simultaneous imaging of total cerebral hemoglobin concentration, oxygenation, and blood flow during functional activation. *Opt Lett*. 28:28-30.
8. Dunn AK, Devor A, Dale AM, Boas DA (2005): Spatial extent of oxygen metabolism and hemodynamic changes during functional activation of the rat somatosensory cortex. *Neuroimage*. 27:279-290.
9. Dunn AK, Bolay H, Moskowitz MA, Boas DA (2001): Dynamic imaging of cerebral blood flow using laser speckle. *J Cereb Blood Flow Metab*. 21:195-201.